

# **CORRUGATED QUANTUM WELL INFRARED PHOTODETECTORS AND ARRAYS**

August 1999

K. K. Choi

U. S. Army Research Laboratory, Adelphi MD 20783

C. J. Chen, L. P. Rohkinson, D. C. Tsui  
Princeton University, Princeton, NJ 08544

N. C. Das, M. Jhabvala  
NASA Goddard Space Flight Center, Greenbelt, MD 20771

M. Jiang, T. Tamir  
Polytechnic University, Brooklyn, NY 11201

## **ABSTRACT**

Quantum well infrared photodetectors (QWIPs) have many advantages in infrared detection, mainly due to the mature III-V material technology. The employment of the corrugation structure further advances the technology by providing a simple, yet efficient light-coupling scheme. A C-QWIP enjoys the same flexibility as a detector with intrinsic normal incident absorption. In this paper, we will discuss the utilities of C-QWIPs in different applications, including two-color detection and polarization-sensitive detection. Besides practical applications, C-QWIPs are also useful in detector characterization. They can be used for measuring the absorption coefficient of light propagating parallel to the layers under bias and providing information on the energy resolved photoconductive gain. These two quantities have never been measured before. Based on the corrugation design, we have made several modifications that further improve the detector sensitivity without increasing its complexity. Other than the C-QWIP structure, we also continue searching for other sensitive detector architectures. In a quantum grid infrared photodetector, 3-dimensional electron confinement can be achieved, with which the detector is able to absorb light in all directions. At the same time, the photoconductive gain can also be improved. We further improve the design using a blazed structure. All the experimental results are supported by a rigorous electromagnetic modal transmission-line theory developed especially for these types of structures. Preliminary thermal imaging using C-QWIP FPAs validates the advantages of the present approach.

## Form SF298 Citation Data

<b>Report Date</b> <i>("DD MON YYYY")</i> 00081999	<b>Report Type</b> N/A	<b>Dates Covered (from... to)</b> <i>("DD MON YYYY")</i>
<b>Title and Subtitle</b> Corrugated Quantum Well Infrared Photodetectors and Arrays		<b>Contract or Grant Number</b>
		<b>Program Element Number</b>
<b>Authors</b>		<b>Project Number</b>
		<b>Task Number</b>
		<b>Work Unit Number</b>
<b>Performing Organization Name(s) and Address(es)</b> U. S. Army Research Laboratory Adelphi MD 20783		<b>Performing Organization Number(s)</b>
<b>Sponsoring/Monitoring Agency Name(s) and Address(es)</b>		<b>Monitoring Agency Acronym</b>
		<b>Monitoring Agency Report Number(s)</b>
<b>Distribution/Availability Statement</b> Approved for public release, distribution unlimited		
<b>Supplementary Notes</b>		
<b>Abstract</b>		
<b>Subject Terms</b>		
<b>Document Classification</b> unclassified	<b>Classification of SF298</b> unclassified	
<b>Classification of Abstract</b> unclassified	<b>Limitation of Abstract</b> unlimited	
<b>Number of Pages</b> 20		

# 1. INTRODUCTION

Quantum well infrared photodetectors (QWIPs) offer a number of advantages in infrared detection. For example, QWIP arrays can be produced in a large-scale format at a low cost and in large quantities. They have small fixed pattern noise. They are free of  $1/f$  noise and offer long-term storage stability. They have excellent linearity characteristics (0.03% per  $^{\circ}\text{C}$ ) over six decades of optical power. The material can be tuned to different wavelengths and bandwidths without degrading the material quality, and offers multi-color capability. These unique features make QWIP to be a serious material system to be considered for infrared detection. However, the basic QWIP material is not responsive to normal incident light, and hence cannot be directly employed in staring focal plane array (FPA) format, for which it needs an additional light-coupling scheme. Therefore, the invention of the basic QWIP material represents only half of what is needed for a viable infrared technology. It still needs an efficient and flexible light coupling mechanism to fully utilize the potentials and the advantages of QWIPs. In this work, we will describe using surface corrugations etched into the QWIP materials for normal incident infrared detection.

## 2. CORRUGATED-QWIPs

In a corrugated quantum well infrared photodetector (C-QWIP), an array of surface corrugations is fabricated into the QWIP active volume using chemical etching process.<sup>1</sup> The sidewalls of the corrugations, which are sustained at a  $50^{\circ}$  angle relative to the layers, reflect normal incident light into nearly parallel direction, and thus allow for infrared absorption. This light coupling scheme turns out to be independent of the incident wavelength and the detector pixel size. One mask design is suitable for the production of a wide variety of FPAs, such as that with different absorption wavelengths, different bandwidths or different wavelength tunability. In addition, the processing of C-QWIP FPAs is extremely simple. The corrugations are created at the same time during pixel delineation. There are no extra processing steps or material layers dedicated to the creation of such a corrugated structure. Under this approach, a QWIP material can even be regarded as a material having intrinsic normal incident absorption for all practical purposes. Fig. 1 shows the typical pixel geometry in a C-QWIP FPA.

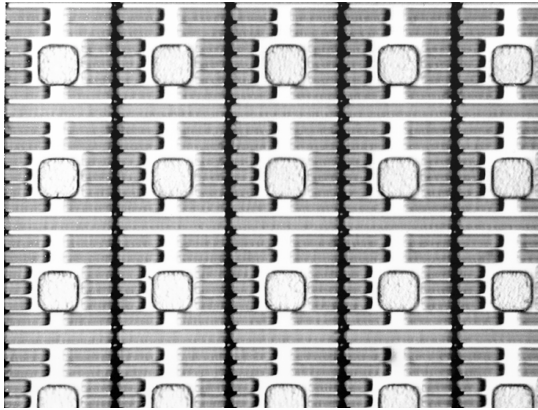


Fig. 1 The figure shows the pixel geometry in a C-QWIP FPA. The pixel size is  $40 \times 40 \mu\text{m}^2$ . There is an unetched island for the top contact metal and an unetched bridge to group several corrugations into one pixel. The size of the unetched island depends on the indium bump size if dielectric isolation is not employed.

Fig. 2 shows the typical spectral responsivity  $R$  of a C-QWIP. The value of  $R$  is about 1.5 times larger than that of the same QWIP under  $45^{\circ}$  edge coupling. There are no appreciable differences in the spectral lineshape between the two coupling schemes. The improvement in  $R$  is consistent with the numerical calculation discussed in a later section. In Fig. 3, we first show the result of this calculation, which is the distribution of the optical intensity  $I_x$  associated with the electric field component  $E_x$  perpendicular to the layers. From this calculation, the average useful optical intensity for infrared

absorption is found to be intensified by a factor of 3.0 compared with that under 45° edge coupling when there is no absorption loss in the medium, i.e. the imaginary part of the dielectric constant  $\epsilon_i = 0$ . Although  $I_x$  is larger in C-QWIPs, nearly half of the active material have been removed under this process. As a result, the theoretical R should only be  $3.0/2 = 1.5$  times larger, consistent with the observed R improvement. To determine the absolute absorption quantum efficiency  $\eta$ , we adjust  $\epsilon_i$  such that it gives the same absorption coefficient  $\alpha$  of a parallel propagating beam in this material, which will also be discussed in a later section. The value of  $\epsilon_i$  turns out to be 0.3, with which  $\eta$  for unpolarized light is  $45\%/2 = 22.5\%$ , again consistent with the results obtained from the characterization of C-QWIP test structures as well as C-QWIP FPAs.

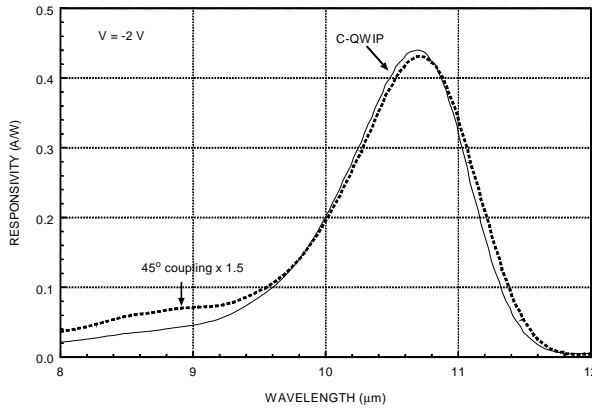


Fig. 2 The spectral responsivity of a C-QWIP and a standard detector. Since a C-QWIP has less active material, it only enhances infrared absorption that is initiated by intersubband transition. This fact indicates that the shoulder observed at  $8.8 \mu\text{m}$  under 45° coupling is not due to intersubband transition.

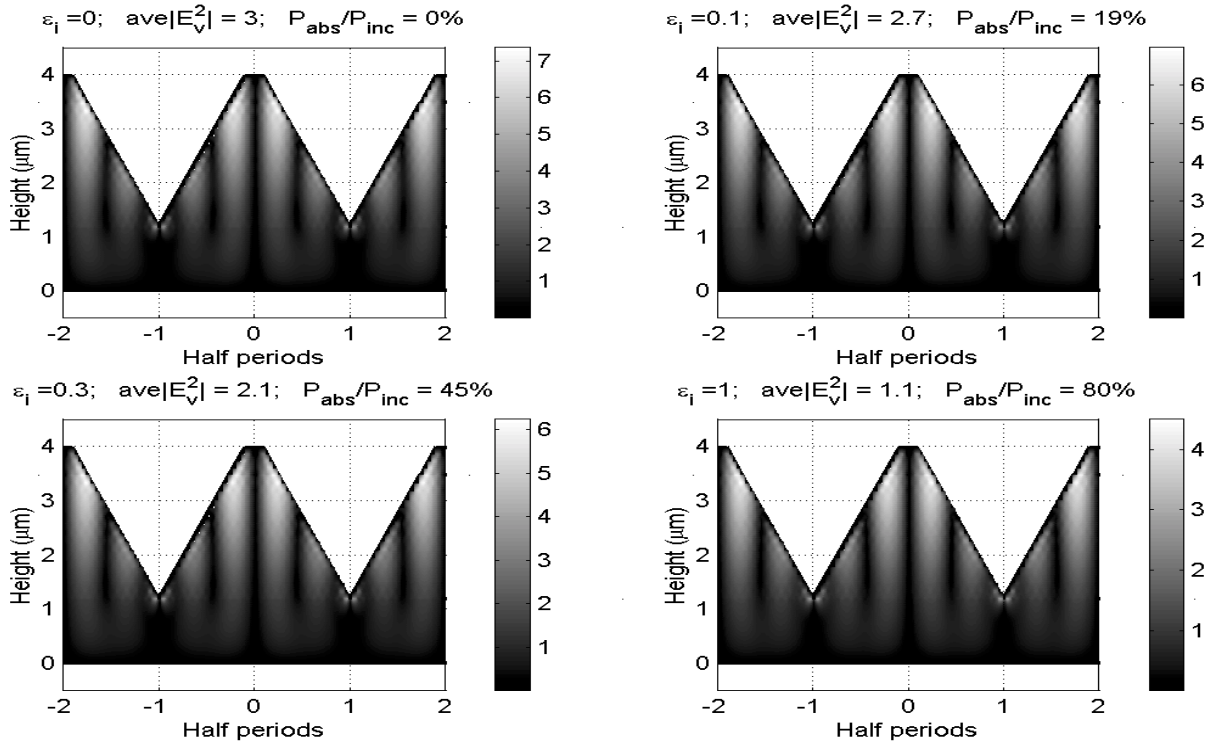


Fig. 3 The  $I_x$  distribution for different  $\epsilon_i$ . The absorption indicated in the figure is for polarized light.

In addition to increasing  $R$ , the C-QWIP structure also reduces the dark current by reducing the amount of active material. As a result, there is additional performance improvement in terms of NE $\Delta T$  according to the expression<sup>2</sup>

$$NE\Delta T = \frac{1}{C} \left[ \frac{2g}{N} \left( 1 + \frac{1}{r_l} \right)^2 + u^2 \right]^{1/2}, \quad (1)$$

where  $C$  is the thermal contrast,  $g$  is the photoconductive gain,  $N$  is the charge capacity of the readout,  $r_l$  is the photocurrent to dark current ratio, and  $u$  is the pixel nonuniformity after correction. Therefore, the overall improvement by C-QWIPs in terms of NE $\Delta T$  is measured by the parameter  $r_l$  or equivalently the responsivity  $NR$  normalized to the same dark current of the edge coupled QWIP. Numerically,  $NR = R(\text{C-QWIP}) \times I_d(45^\circ) / I_d(\text{C-QWIP})$ . On the average,  $r_l$  is improved by a factor of 3.2 in the 4 to 18  $\mu\text{m}$  wavelength range.<sup>1</sup> The improved  $r_l$  increases the background limited temperature  $T_{\text{BLIP}}$ , defined as the temperature at which  $r_l = 1$ . Fig. 4 shows the improvement on  $T_{\text{BLIP}}$  using C-QWIPs as a function of the cutoff wavelength  $\lambda_c$ , defined at the half maximum. The figure shows that  $T_{\text{BLIP}}$  is 77 K for  $\lambda_c = 9 \mu\text{m}$ .

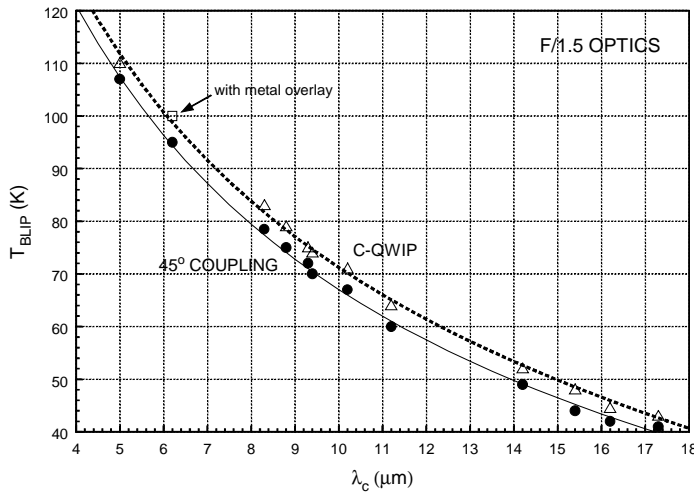


Fig. 4 The background limited temperature of C-QWIPs and the monitoring detectors at different cutoff wavelengths. There is a 30% transmission loss through the dewar window.

### 3. C-QWIPs for TWO-COLOR DETECTION

Since the corrugated structure is able to provide uniform coupling to different wavelengths, it is particularly suitable for broadband detection or voltage tunable infrared detection. The need for a wavelength-independent light coupling scheme is accentuated in performing detection at two widely separated spectral bands. This detection capability is essential in precision remote temperature sensing.<sup>3</sup> It is designed to improve the temperature resolution and to eliminate the emissivity variation of the targets. Fig. 5 shows the normalized responsivity  $NR$  of a C-QWIP with two stacks of quantum wells, each sensitive in a specific spectral band. There are three contacts in the detector to monitor the individual photocurrent simultaneously. Note that in this particular detector, more active material is removed from the upper QW stack, which is for the long-wavelength band, than the lower stack. Therefore, the photocurrent enhancement and the dark current reduction are very different for the two QW stacks. Yet, the normalized responsivity is very similar in both bands. This result shows that the performance of a C-QWIP is not sensitive to its structural parameters such as the corrugation period or the etching depth, and uniform enhancement can be obtained in both bands within a single C-QWIP pixel for sensitive two-color detection.

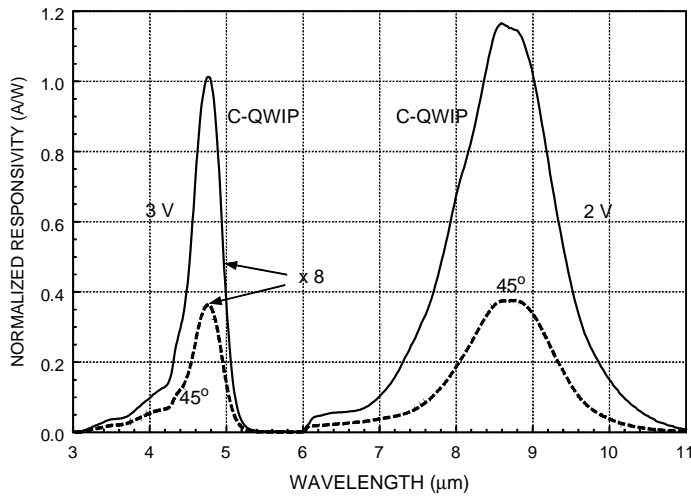


Fig. 5 The normalized responsivity of a C-QWIP having two QW stacks. The data show similar NR improvements relative to the monitoring detector despite the very different locations of the two QW stacks within the corrugation.

By taking the ratio of the photocurrent generated in the MW band to that in the LW band, the emissivity of a target can be eliminated, and its temperature can be readily acquired by knowing the detector spectral responsivity in the respective bands. We have used the present detector for precision temperature measurement. Since the present experimental setup is not for imaging, an optical chopper is employed to measure the temperature of a particular target, which in this case is a calibrated blackbody point source. Fig. 6 shows the measured photocurrent ratio between the two bands as a function of the blackbody setting temperature. It also shows the calculated ratio from the responsivity data and the known blackbody radiation spectrum without a fitting parameter. There is good agreement between the theory and the experiment, indicating that the C-QWIP is capable of precision temperature sensing. By measuring the photocurrent ratio, the temperature of the target can be directly read off from Fig. 6. Without a chopper, we have also used the detector to measure the extended room temperature background using the dc background photocurrents, and obtained accurate reading. Therefore, we have shown that once the spectral responses of the detector are known, the detector can be used for measurements at any temperature range without further calibrations.

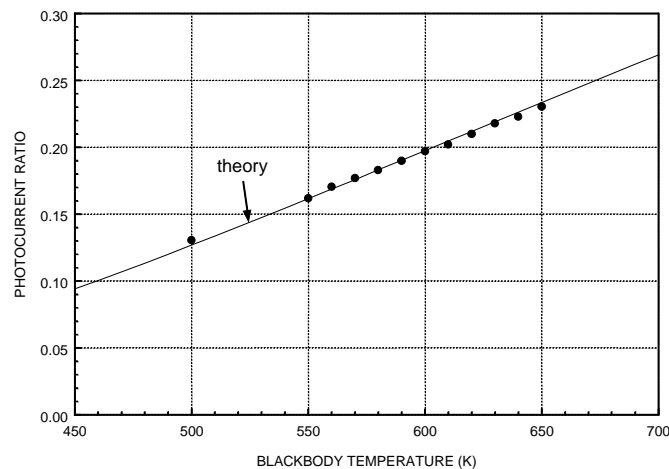


Fig. 6 The measured photocurrent ratio (circles) and the calculated value (solid curve) as functions of temperature.

## 4. C-QWIPs FOR POLARIZATION-SENSITIVE DETECTION

In certain circumstances, the utility of IR imaging is limited by the low thermal contrast, such as in land mine detection. On the other hand, the polarization of thermal radiation can have high contrast, depending on the nature of the target and the background. For example, the radiation from a rocket plume is unpolarized but the reflection of this radiation from the rocket hardbody can be highly polarized. The use of IR detectors which can capture both polarization and intensity data will lead to significant improvement in target recognition functions.

Since C-QWIPs with linear corrugations are sensitive to only one polarization, which is the s-polarization. C-QWIPs with different corrugation orientations can be used to detect both the intensity and the polarization of an incoming radiation. It turns out that a set of four C-QWIPs with four different orientations is needed to completely characterize the polarization-state of a radiation.<sup>4</sup> We have fabricated four C-QWIPs oriented at  $90^\circ$  (detector A),  $0^\circ$  (detector B) and  $\pm 45^\circ$  (detector C) relative to the [011] axis. Since the sidewall profiles of the corrugations with different orientations are different, the sensitivity of each detector is also different. However, such a difference does not affect the polarization detection. Fig. 7 (a) shows the photocurrent of the detectors generated by a common blackbody source. A linear polarizer is placed in front of the source to study the photocurrent of each detector with different

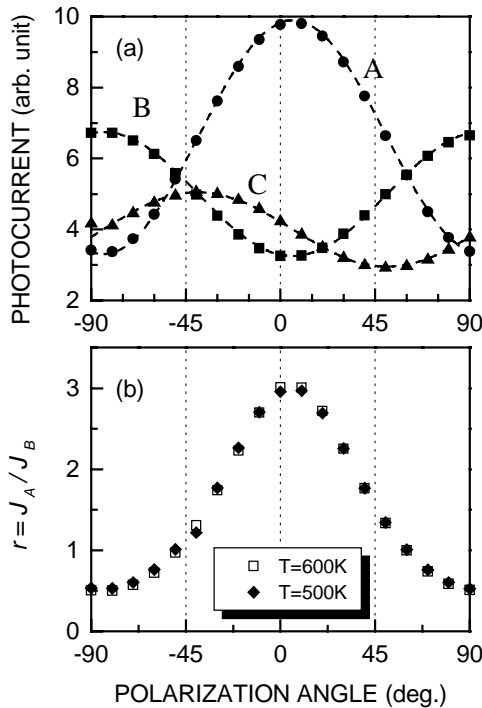


Fig. 7 (a) shows the C-QWIP photoresponse with orientation at  $0^\circ$  (squares),  $90^\circ$  (circles) and  $+45^\circ$  (triangles). C-QWIPs with  $\pm 45^\circ$  have the same photoresponse. C-QWIPs with  $90^\circ$  orientation (detector A) is the usual structure being used. (b) The ratio of the photocurrents from A and B as a function of polarization angle. This ratio is independent of the incident intensity if the radiation is linearly polarized.

polarization angle relative to the [011] axis. As expected, the magnitude of the signal from detectors A and B is  $90^\circ$  out of phase since the corrugations are orthogonal to each other. If we take the photocurrent ratio  $r = J_A/J_B$  from these two detectors, it is maximized at the polarization angle  $\theta = 0^\circ$  and decreases toward  $\pm 90^\circ$  as shown in Fig. 7 (b). This ratio is independent of the target intensity as the figure shown for two blackbody temperatures. This  $r$  contrast remains at a ratio of 6 for the two polarizations. Therefore, from the value of  $r$ , one can determine the angle  $\theta$  up to the sign of the angle. However, this

simplified scheme of using only two C-QWIPs instead of four can determine the polarization only when the radiation is purely linear polarized.

When the radiation is partially polarized, the ratio  $r$  depends partly on the degree of polarization, i.e. the ratio of the polarized component vs. the total intensity, and partly on  $\theta$  of the polarized component. Nevertheless this simplified scheme is still useful in obtaining a finite contrast from a scene which does not show an intensity contrast, provided that there is a finite degree of polarization in the radiation. It can be used in certain target recognition function that does not require complete knowledge of the polarization-state. For example, Table 1 is a record of  $r = J_A/J_B$  for light reflected off from a material surface, which is illuminated by a chopped, unpolarized blackbody source. Table 1 shows  $r$  different for different materials, based on which the nature of the material may be identified. If we regard the reflected light were linearly polarized, we could also obtain the corresponding value of  $|\theta|$  from Fig. 7 (b). The value of  $|\theta|$  is also shown in Table 1. It spans from  $48.6^\circ$  to  $79.2^\circ$  for the materials tested, which indicates a rather wide range of values. Note that although the value of  $\theta$  helps us to visualize the sensitivity of the present detection scheme, it does not indicate the actual  $\theta$  of the polarized component in the radiation since the degree of polarization of the reflected light is not known. The maximum error occurs when the reflected light is totally unpolarized, with which  $\theta$  is interpreted as  $45^\circ$ .

MATERIAL	$J_A/J_B$	$\theta$ (Degree)	MATERIAL	$J_A/J_B$	$\theta$ (Degree)
Gold	1.41	48.6	Tree Bark	0.805	67.3
Painted Aluminum	0.605	78.3	Leaf	0.683	73.4
Bare Aluminum	1.36	49.8	Glass Plate	0.844	65.7
Paper	0.694	72.7	Mirror	0.759	65.1
Cloth	0.983	60.6	Plastics	0.594	79.2

Table 1 The photocurrent ratio of two C-QWIPs with corrugation orientations orthogonal to each other. Both the illumination and the detection are at  $45^\circ$  relative to the normal of the reflecting surface.

Fig. 8 is a proposed polarization-sensitive FPA pixel geometry for the simplified detection scheme. It should be noted that the P-S FPA processing remains to be simple, involving only one chemical etching step and one metalization step before the indium bump bonding processing. Other than providing the information for  $r$ , the FPA can also be used to obtain separate IR intensity imageries for each of the two polarizations.

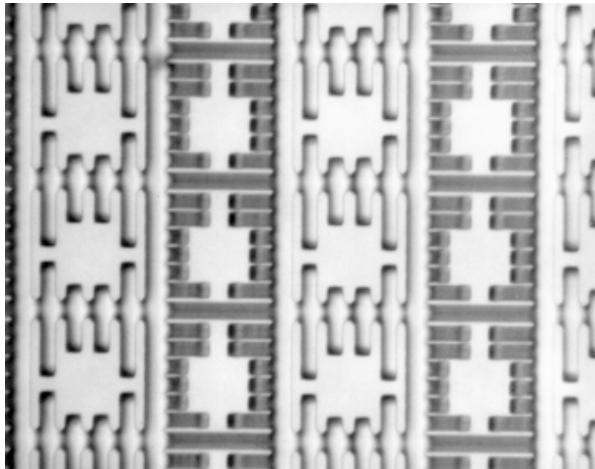


Fig. 8 The figure is the top view of a polarization-sensitive FPA after chemical etching to create the corrugations. Notice the very different corrugation profiles for the two orientations. The side view reveals that one has an upright triangular profile, and the other has an inverted triangular profile.



## 5. C-QWIPs FOR DETECTOR CHARACTERIZATION

In this section, we will use the same surface corrugations in a C-QWIP structure as a probing tool to measure the absorption coefficient  $\alpha$  and the photoconductive gain  $g$  of a QWIP material. This technique can be applied to different material structures and different operating conditions, and hence it provides more accurate and relevant information on the intrinsic detector properties. With this information, detector performance can be more accurately assessed and optimized.

To characterize the optical properties of a QWIP in the past, one usually measures the responsivity  $R$ , from which the product of  $\eta$  and  $g$  is deduced, where  $\eta$  is the quantum efficiency under a specific light-coupling scheme. These parameters are related by

$$R = \frac{e}{h\nu} \cdot \eta \cdot g \quad , \quad (2)$$

where  $h\nu$  is the incident photon energy. If one of the two parameters,  $\eta$  or  $g$ , can be measured accurately, the other can be determined using Eq. (2). However, there are difficulties in measuring either of these two quantities. For example, to obtain the value of  $\eta$ , one usually measures the infrared absorption of the material using a Fourier transform infrared spectrometer. Typically, the measurement is performed on a large unprocessed, unthinned sample, at room temperature without an applied bias, and with light incident at the Brewster angle or on a  $45^\circ$  facet. These measurement conditions are far from that of a detector pixel in a thinned detector array, operated at cryogenic temperatures, with a bias, and under normal incident condition. Furthermore, in some situations where intersubband absorption is weak or background transmission loss is large, accurate measurements can be difficult.

Similarly, to determine the photoconductive gain, the usual approach is to perform current noise measurements. However, there are fundamental differences between the photoconductive gain and the noise gain for QWIPs. They are not theoretically identical. Furthermore,  $g$  varies with the energy of the charge carriers. The noise gain obtained in these measurements is only an average value, depending on the average energy of the carriers in the conducting current. It thus depends on the measuring conditions, such as the sample temperature or the energy of the background photons. The measured average gain cannot be uniformly applied across the entire absorption spectrum. In order to properly characterizing the properties of a QWIP, the knowledge of  $g$  as a function of electron energy is required.

In the present approach, a batch of C-QWIPs with different V-groove periods is prepared. The side view of a C-QWIP having four corrugation units is illustrated in Fig. 9. Upon chemical etching, the sidewalls of these corrugations are inclined at about  $50^\circ$  relative to the layers. Consequently, the normal incident light reflected at these sidewalls travels nearly parallel ( $15^\circ$ ) to the layers, as occurred under an efficient light coupling scheme. The s-polarization of the incident radiation can then be absorbed and decays exponentially as light propagates away from these sidewalls. Since the detector substrates are partially thinned, the measured absorption also includes any possible waveguiding effect of the substrate.

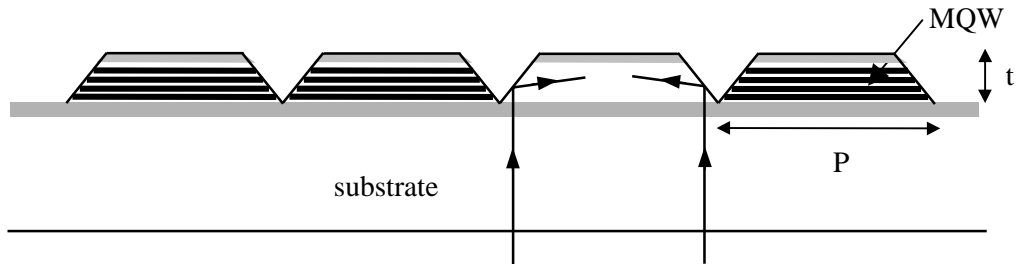


Fig. 9 The profile of a C-QWIP with etching depth  $t$  and corrugation period  $P$ .

If we assume the light reflected from the opposite sidewalls interferes incoherently, we can write  $I(x) = I_0 \exp(-\alpha x)/2$ , where  $I$  is the intensity of the s-polarized light away from an edge,  $I_0$  is the unpolarized incident intensity, and  $x$  is measured along the layers.

Due to optical absorption, the unpolarized responsivity  $R$  for a C-QWIP with period  $P$  is given by

$$R(P) = \frac{e}{h\nu} \cdot g \cdot \eta(P) = \frac{e}{h\nu} \cdot g \cdot \frac{\alpha}{2 \cdot P} \cdot \int_0^t \int_0^{P-2 \cdot z} e^{-\alpha \cdot x} + e^{-\alpha \cdot (P-2 \cdot z-x)} dx dz + R_o, \quad (3)$$

$$= \frac{e}{h\nu} \cdot g \cdot \frac{1}{P} \cdot \left[ t + \frac{e^{-\alpha \cdot P}}{2 \cdot \alpha} (1 - e^{2 \cdot \alpha \cdot t}) \right] + R_o,$$

where  $t$  is the etching depth and  $R_0$  is a constant.  $R_0$  accounts for a finite detector photoresponse observed even when  $P$  is large, and hence it is not produced by sidewall reflection. The definition of  $\eta(P)$  in Eq. (3), which measures the total optical signal from a detector, includes this additional photoresponse.  $R_0$  can be due to the presence of random surface scattering and the coupling of the p-polarized light by the two of the four mesa edges. The value of  $R_0$  can be obtained from the responsivity of a large area detector without corrugations. As a function of  $P$ ,  $R(P)$  is expected first increasing with  $P$  since there is more material within a corrugation unit to absorb light. However, when  $P$  increases beyond  $1/\alpha$ , the material at the center of a corrugation unit receives little or no reflected light, while the total number of reflecting sidewalls in the detector is reduced.  $R(P)$  thus decreases. The functional form of  $R(P)$  is therefore determined by  $\alpha$ . The remaining prefactor  $g$  in Eq. (3) determines the overall magnitude of  $R$ . Therefore, by fitting  $R(P)$  as a function of  $P$ , the values of  $\alpha$ ,  $g$ , and  $R_0$  can be uniquely determined.

Alternatively, one can also fit the normalized responsivity  $NR(P)$  as a function of  $P$ .  $NR(P)$  is  $R(P)$  times the dark current ratio of the monitoring QWIP and a C-QWIP at certain operating temperature. Theoretically, the dark current ratio is simply inversely proportional to the reduction of the average surface area after etching, and is equal to  $P/(P-t)$ . Therefore,  $NR(P)$  is given by

$$NR(P) = \frac{e}{h\nu} \cdot g \cdot \frac{1}{P-t} \cdot \left[ t + \frac{e^{-\alpha \cdot P}}{2 \cdot \alpha} (1 - e^{2 \cdot \alpha \cdot t}) \right] + R_o \cdot \frac{P}{P-t}. \quad (4)$$

Different from  $R(P)$ ,  $NR(P)$  depends only on the average optical intensity in the corrugation and not on the amount of active material remained. As a result,  $NR$  is always a decreasing function of  $P$ . In this work we will use  $NR(P)$  in Eq. (4) for fitting because this value also indicates the detector performance for different  $P$ . The reason we can assume incoherence of light in the fitting is due to the fact that coherence interference will only redistribute the local intensity but will not change the spatially averaged intensity, which  $R$  and  $NR$  depend on. In the following, we will first show the result for a LW detector material and then a MW detector material.

The LW sample we used for this illustration consists of 40 periods of QWs. The thickness of the active region is  $2.25 \mu\text{m}$ . On top of this material, there is a  $0.5 \mu\text{m}$  thick GaAs contact layer. Therefore, a total depth of  $t = 2.8 \mu\text{m}$  has been etched to expose the active volume. The doping density in the well is  $5 \times 10^{17} \text{ cm}^{-3}$ . In the experiment, a total of ten C-QWIP samples, with period  $P$  varying from  $6 \mu\text{m}$  to  $1200 \mu\text{m}$ , were used. Although the samples can be characterized at different temperatures to reveal the temperature dependence, we report here only results obtained at  $77 \text{ K}$ , the temperature at which most of the LW C-QWIPs are background limited.

Fig. 10 shows the spectral  $NR$  curves for all the C-QWIPs with different  $P$ . The applied bias on the substrate is  $2 \text{ V}$ , the normal operating voltage of the detectors. As expected, the value of  $NR$  is larger

for a smaller  $P$ . NR for  $P = 6 \mu\text{m}$  is a factor of 10 larger than that with  $P = 1200 \mu\text{m}$ ; it is also a factor of

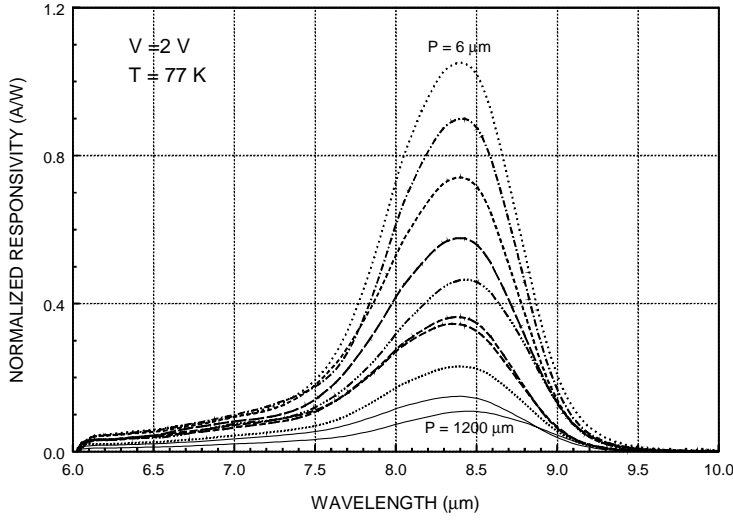


Fig. 10 The normalized responsivity of C-QWIPs having  $P = 6, 8, 10, 15, 20, 30, 40, 60, 300$ , and  $1200 \mu\text{m}$  in the descending order.

2.2 larger than that with the  $45^\circ$  edge coupling for this particular sample.

From Fig. 10, we can extract the value of NR at a fixed wavelength for different  $P$ . Fig. 11 shows the  $P$  dependence at different locations of the spectrum. In the same figure, we also plot the fitting to Eq. (4) using  $\alpha$ ,  $g$  and  $R_0$  as the fitting parameters. The figure indicates that the data generally fall onto the fitting curves closely, confirming the underlying physical picture of infrared absorption in QWIPs. The facts that NR decreases monotonically with  $P$  and there is little change in the spectral lineshape for different  $P$  indicate the effects of coherent interference of light are small, either between the two opposite sidewalls within a corrugation or among different corrugations.

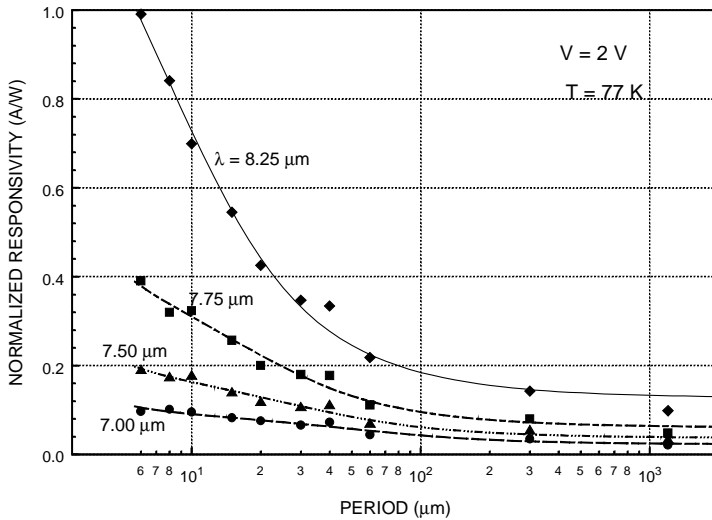


Fig. 11 The normalized responsivity as functions of  $P$  at four different wavelengths and their fits to Eq. (4).

Using the fitted parameters, one can obtain the quantum efficiency  $\eta$  from Eq. (3) for different C-QWIP structures at 2 V bias. The result is shown in Fig. 12. Unlike NR,  $\eta(P)$  is peaked at a certain value of  $P$ , depending on  $\alpha$  at that particular wavelength. For a large  $\alpha$  at  $\lambda = 8.25 \mu\text{m}$  which is near the absorption peak,  $\eta$  is peaked at a small  $P$ . But when the absorption is weak near the tail, a larger period is

needed to obtain the maximum  $\eta$ . Since the functional dependence of  $\eta$  and NR on  $P$  is different, there is a difference in the design rules for detector optimization, especially for the weak absorption material. To optimize NR, a small  $P$  is always preferred. On the other hand, a larger  $P$  may give a larger  $\eta$ . For the present material, the deduced  $\eta$  is 27 % at  $P = 6 \mu\text{m}$  and 29 % at  $P = 8 \mu\text{m}$  at the absorption peak, which has included a finite contribution from  $R_0$ . These values are consistent with the theoretical value of  $\eta = 22.5 \%$  for  $P = 5.5 \mu\text{m}$  without the contribution of  $R_0$ , calculated from the rigorous electromagnetic modeling for the same  $\alpha$ . Therefore, we have determined the internal quantum efficiency of an optimized C-QWIP is about 27 % from both theoretical and experimental considerations. We emphasize that the present approach of deducing  $\alpha$  from the shape of the NR( $P$ ) curve is independent on the system calibration. It depends only on the precision of the period lengths in the fabrication mask; and therefore it is reliable.

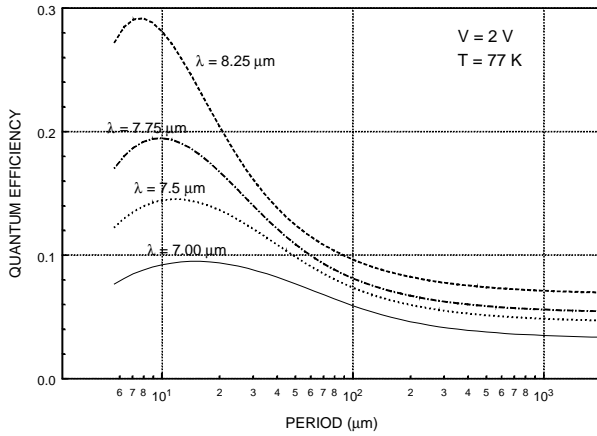
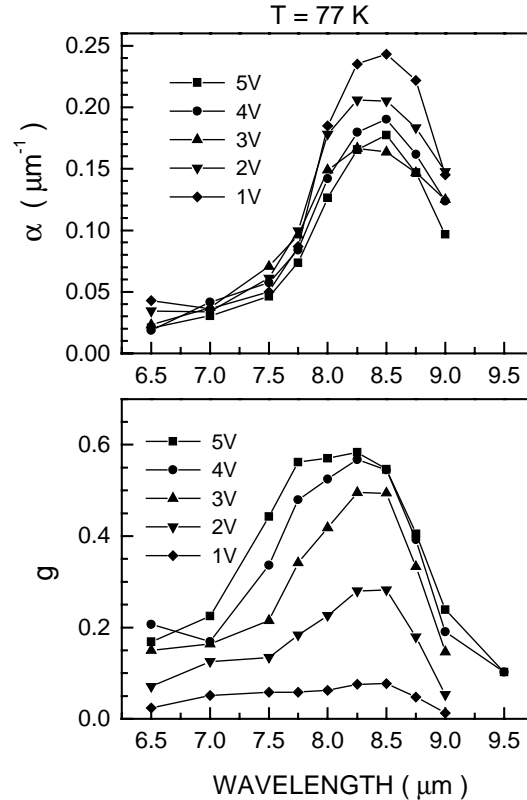


Fig. 12 The deduced quantum efficiency of C-QWIPs with different periods at different parts of the absorption spectrum.

At the absorption peak, the spectral responsivity  $R$  of the C-QWIP with  $P = 6 \mu\text{m}$  is measured to be 0.15 A/W at 1 V and 0.94 A/W at 5 V. In the past, this  $R$  increase would be exclusively attributed to the change of  $g$  while  $\alpha$  is assumed to be independent of  $V$ . Under the present approach, both  $\alpha$  and  $g$  can be monitored simultaneously as a function of  $V$ . Fig. 13 shows the results of these two parameters from the curve fitting. Despite the increase of  $R$  with  $V$ , the absorption coefficient  $\alpha$  actually decreases, up to 38 % at 5 V. This decrease can be explained by the carrier depletion in the QWs in the presence of an applied bias. The absorption is peaked at around  $8.5 \mu\text{m}$ , same location as the  $R$  peak, at which  $\alpha = 0.22 \mu\text{m}^{-1}$  at 2 V, corresponding to a decay length of  $4.5 \mu\text{m}$  for the parallel

Fig. 13 The deduced parameters  $\alpha$  and  $g$  as functions of wavelength for different applied biases.



propagating light. The parameter  $g$ , on the other hand, increases monotonically with  $V$  as expected. At 1 V,  $g$  is approximate a constant across the spectrum. However, as  $V$  increases, the value of  $g$  increases rapidly around the excitation wavelength of 8.5  $\mu\text{m}$ , creating a strong peak at large bias. This peak is created because at longer  $\lambda$ , the small photoelectron energy limits the carrier lifetime. At shorter  $\lambda$ , the acceleration of photoelectrons to the higher energies initiates intervalley scattering and thus reduces electron mobility. Both factors prevent a large  $g$  at both ends of the spectrum. We plot the peak value of  $g$  as a function of bias in Fig. 14, along with the noise gain of the background photocurrent and the 77 K dark current, respectively. At low bias, the three parameters are nearly the same because the value of  $g$  is insensitive to the electron energy as shown in Fig. 13. At high bias, the three parameters become different. The noise gain of the dark current is smaller than that of the background photocurrent, which is in turn smaller than the peak value of the photoconductive gain. Fig. 13 shows that at large bias, the value of  $g$  is very sensitive to the electron energy. Since the dark current composes mostly thermally assisted tunneling current at high bias, its conducting electrons have the lowest energy distribution, and hence have a smallest average gain. The background photocurrent is generated by 300 K blackbody radiation, whose photon flux increases with  $\lambda$  between 6 to 10  $\mu\text{m}$ . As a result; most photoelectrons are created with energies below its absorption peak. The average noise gain of the photocurrent is thus less than the peak value. Note that at 5 V, the photocurrent noise gain  $g_n$  and the peak photoconductive gain  $g_p$  can differ by a factor of two. If one uses  $g_n$  instead of  $g_p$  in Eq. (2) to estimate  $\eta$  at the peak, one will get  $\eta = 46\%$  instead 25 % for the present C-QWIP with  $P = 6\ \mu\text{m}$  at 5 V. Therefore, the conventional approach can introduce substantial error at large bias.

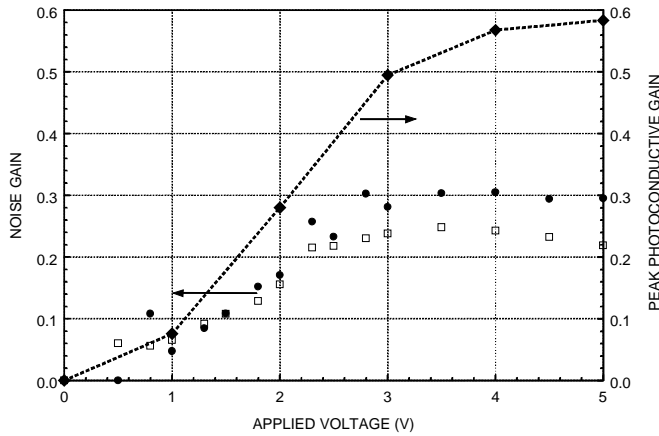


Fig. 14 The figure shows the noise gain measured on the 77 K dark current (squares) and the 300 K background photocurrent (circles) as functions of bias. It also shows the peak value of photoconductive gain deduced from the curve fitting. Their values are increasingly different at large bias.

One can also apply the same characterization technique to a MW detector. The active material consists of 20 periods of 300-Å  $\text{Al}_{0.4}\text{Ga}_{0.6}\text{As}$  barriers and 5-Å  $\text{GaAs}/25\text{-}\text{\AA}\ \text{In}_{0.28}\text{Ga}_{0.72}\text{As}/5\text{-}\text{\AA}\ \text{GaAs}$  wells. The doping density in the InGaAs layer is  $2.0 \times 10^{18}\ \text{cm}^{-3}$ . The total active material thickness is 7000 Å. On top of this material, there is a thick (1.8  $\mu\text{m}$ ) GaAs contact layer. With this thick contact layer, a total depth of  $t = 2.8\ \mu\text{m}$  has been etched to expose the active volume. Since the contact layer has negligible infrared absorption, portions of the reflected light path within the corrugations are in the non-absorbing region, resulting in a smaller  $\alpha$  than that if the entire volume were filled with the active material. Therefore, the deduced  $\alpha$  in this example should be viewed as the average absorption coefficient of an inhomogeneous medium, which consists of the quantum wells and the contact layer. The smaller  $\alpha$  will give a smaller  $\eta$  in Eq. (3), which is consistent with the fact that the smaller number of QW periods in the present detector material will have a smaller  $\eta$  when compared with that of a detector having more QW periods in the corrugations. Fig. 15 shows the spectral responsivity  $R$  of several C-QWIPs measured at 110 K, which is the  $T_{\text{BLIP}}$  of the  $P = 8\ \mu\text{m}$  C-QWIP.

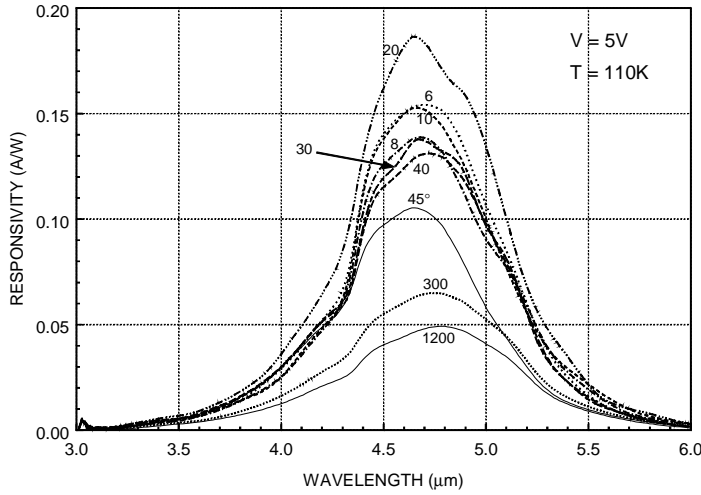


Fig. 15 The spectral responsivity  $R$  of C-QWIPs with different  $P$ .

The parameters  $\alpha$  and  $g$  deduced at different  $V$  and  $\lambda$  are shown in Fig. 16. In this case,  $\alpha$  is peaked at  $4.5 \mu\text{m}$ , which is somewhat shorter than that of the  $R$  maxima in Fig. 15. This discrepancy is due to the fact that  $g$  is peaked at a different  $\lambda$  of  $4.7 \mu\text{m}$ . Nevertheless, the  $\alpha$  maximum explains the appearance of a shoulder at  $4.5 \mu\text{m}$  in the spectral response curves. While the spectral shape and the voltage dependence of  $g$  are similar to that of the LW detector and can be explained by similar effects, the voltage dependence of  $\alpha$  is opposite to that of the LW detector. The value of  $\alpha$  is double when  $V$  increases from 1 to 5 V. We attribute this effect to the increased electron density in the QW caused by the field ionization of donors in the barrier region. Due to the heavy doping in the present QWs and the large Al molar ratio of the barriers, significant amount of dopants can diffuse into the barriers and form deep donor levels. The transfer of electrons from these donor levels to the QWs under bias increases  $\alpha$ . As discussed before,  $g$  is a strong function of energy. There will be a substantial error if one assumes  $g$  to be a constant throughout the spectrum at large bias. The noise gain  $g_n$  of the background photocurrent in this case is measured to be 0.17 at 5 V, which is 3 times less than the peak value of  $g$ . The

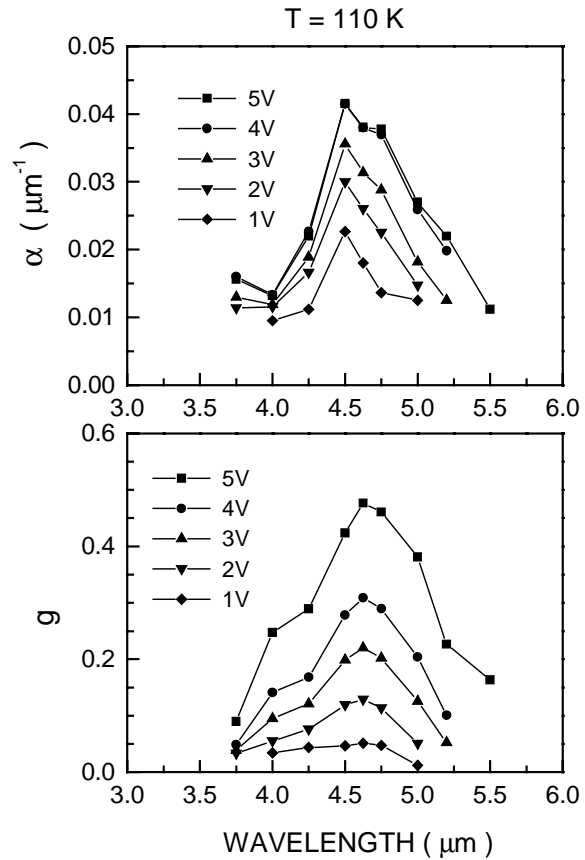


Fig. 16 The deduced parameters  $\alpha$  and  $g$  as functions of wavelength for different applied biases.

larger difference in  $g_n$  and  $g_p$  is due to the more rapid increase in the photon flux with wavelength in the MW regime. Substituting the fitted parameters into Eq. (3), we found that the peak  $\eta = 9.3\%$  at  $V = 5\text{ V}$  for  $P = 15\text{ }\mu\text{m}$ . Again, if we used  $g_n$  to evaluate  $\eta$  as in the conventional approach, we would overestimate  $\eta$  by a factor of 3 at high bias. When  $g_p$  and  $g_n$  are different, the 300 K background limited detectivity is proportional to  $\sqrt{(g_p/g_n)}$  instead of independent of  $g$ . For  $\alpha = 0.04\text{ }\mu\text{m}^{-1}$ , the corresponding decay length in this detector material is  $25\text{ }\mu\text{m}$ . We expect a smaller decay length and a higher quantum efficiency if the sample contains more QW periods.

In this section, we have demonstrated a simple yet powerful characterization technique for QWIPs. Since the deduced  $\alpha$  and  $\eta$  are for parallel propagating light in thinned substrate under typical operating conditions, the technique also gives more realistic information on the actual detector performance.

## 6. OTHER C-QWIP DESIGNS

In this section, we discuss some variations of C-QWIP designs due to practical considerations of small pixel size in high resolution FPAs.

### 6.1. C-QWIPs with dielectric coverage

Despite the improved performance of C-QWIPs, there is a technical issue in relation to the pixel size. In the present design of  $40 \times 40\text{ }\mu\text{m}^2$ , there is a  $15 \times 15\text{ }\mu\text{m}^2$  unetched area for indium bonding. The bonding area constitutes 14 % of the total area. For a smaller pixel size, the bonding area needs to be scaled down proportionally. For example, the bonding area would be  $11 \times 11\text{ }\mu\text{m}^2$  for a  $30 \times 30\text{ }\mu\text{m}^2$  pixel, which may require special indium bonding techniques.

In order to solve the bonding area requirement, we have investigated several dielectrics for contact isolation.<sup>5</sup> With a thin dielectric film covering the entire pixel except the contact area, the bonding area of a C-QWIP pixel can be made much smaller, in the order of  $5 \times 5\text{ }\mu\text{m}^2$ . Moreover, the ohmic metal layer can now be extended to cover the entire corrugated active area. The metal layer reflects all the light back into the detector active region, which tends to further increase the detector responsivity beyond that offered by the GaAs-air interface. The cross section of a pixel structure with dielectric and metal coverage is shown in Fig. 17.

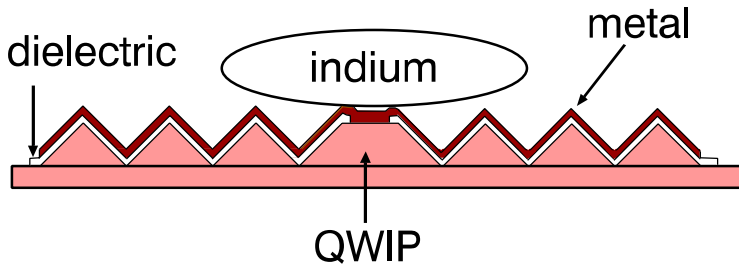


Fig.17 The cross section of a C-QWIP with dielectric and metal coverage.

The most common dielectric in IC fabrication is  $\text{SiO}_2$ . The conformal nature of the dielectric coverage makes the material attractive in the present application. We have fabricated C-QWIPs with different periods  $P$  using  $\text{SiO}_2$  as an insulating dielectric for complete metal coverage. Fig. 18 shows the normalized responsivity NR achieved under this approach. For the smallest  $P = 8\text{ }\mu\text{m}$  tested, NR has been increased by 5.4 times compared with that using edge coupling. This result shows that complete metal coverage will increase detector performance, in addition to solving the contacting problem.

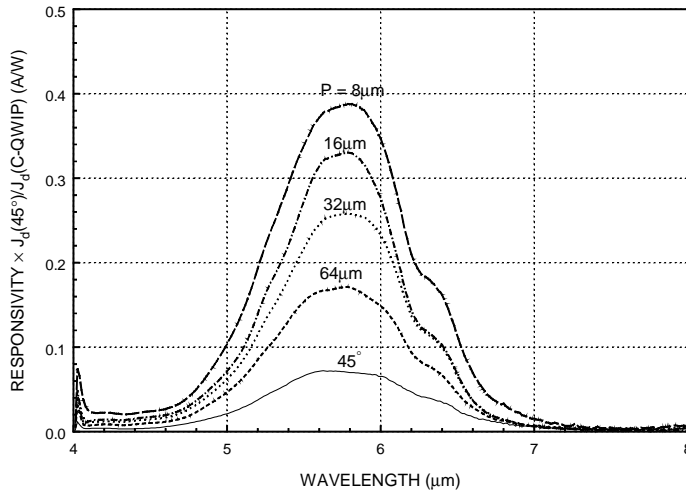


Fig. 18 The normalized responsivity of C-QWIPs with different periods  $P$  having  $\text{SiO}_2$ /metal coverage.

Despite  $\text{SiO}_2$  is ideal for MW and very long wavelength detectors, it turns out that the material is highly absorbing in the 8-10  $\mu\text{m}$  range. LW C-QWIPs made of this material show only comparable performance as the edge-coupled detector. For improved performance, other non-absorbing dielectric materials have to be sought. We have tested ZnS as the dielectric for the LW detectors. Fig. 19 shows the responsivity  $R$  of C-QWIPs having ZnS as a dielectric insulating layer.

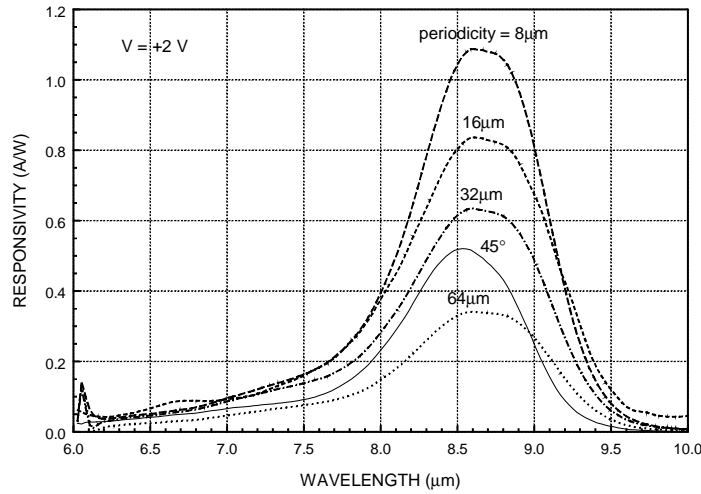


Fig. 19 The responsivity  $R$  of C-QWIPs having ZnS as a dielectric insulating layer.

With ZnS/metal coverage,  $R$  is enhanced by 2.7 times instead of the average 1.5 times observed without the dielectric coverage. This result shows the potential of using dielectrics and metal coverage to enhance detector performance. However, the ZnS film deposited on C-QWIPs shows slight leakage current, leading to a smaller reduction in the dark current. For example, the dark current for the  $P = 6 \mu\text{m}$  C-QWIP is 90 % of that of the monitoring QWIP, substantially less than a factor of two reduction. It turns out that the ZnS film is less conformal to the corrugated surfaces. Some of the sidewall areas of the corrugated grooves are not well covered by the dielectric in the deposition, which produces a small leakage current. Therefore, the present characteristics of the dielectric are not intrinsic to this material but are related to the deposition techniques. Better result is expected if deposition procedures are modified to provide more uniform dielectric coverage on the detector structure.



## 6.2. C-QWIPs with center vertical trenches

Either based on EM field calculation or based on parity symmetry of EM interaction, one can conclude that the optical intensity associated with the perpendicular electric component  $E_x$  is necessarily identical to zero at the center of any symmetric corrugation profile, if the radiation is coherent. Therefore, the center region produces no photocurrent, and better detector performance may be achieved if this region is removed. Another consideration is the corrugation period in relation to the pixel size. For small pixel sizes, a C-QWIP with a fixed period  $P$  may not be able to fit into the pixel area. In order to improve the detector sensitivity and flexibility, we studied C-QWIPs with a vertical trench etched into each corrugation unit using anisotropic etching techniques. In FPAs with small pixel pitches, anisotropic etching using plasma is preferred to separate FPA columns in order to preserve pixel material. Therefore, the trenches can be created during column separation without introducing extra steps. Fig. 20 shows the NR of a  $P = 10 \mu\text{m}$  C-QWIP with trenches that are  $2 \mu\text{m}$  wide, in comparison with that without trenches. In comparison with the same  $P$ , the one with trenches has a 44 % higher NR at  $V = 5 \text{ V}$ . Even compared with a regular C-QWIP with a smaller  $P$  of  $6 \mu\text{m}$ , there is a 15 % improvement at 5 V. This result shows that the performance of a C-QWIP can be improved by additional trenches. It is particularly useful when the pixel pitch can only fit one or two corrugation units. This experiment shows that coherent interference does occur within a corrugation even though it does not affect the average intensity in a C-QWIP.

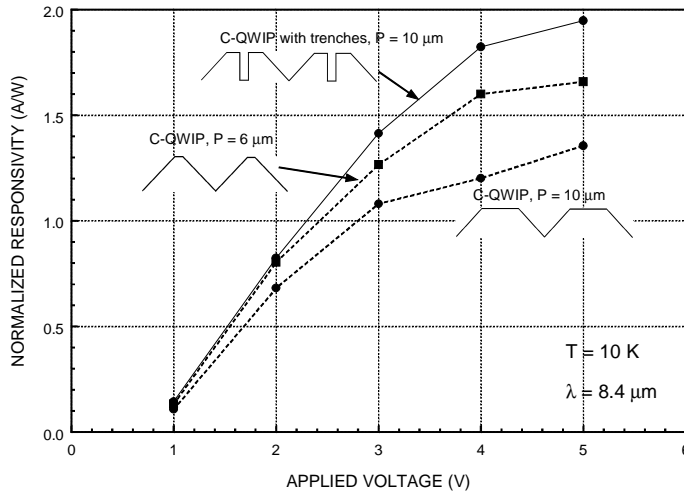


Fig. 20 The figure shows NR of a C-QWIP with vertical trenches at the centers in comparison with that without trenches. Note that since the new structure remains symmetrical, the optical intensity at the centers of the trenches is still zero.

## 7. QUANTUM GRID INFRARED PHOTODETECTORS

In the previous sections, we have shown that the employment of the corrugated light coupling scheme adds simplicity, versatility and sensitivity to the QW infrared technology. To further advance the technology, intense efforts have been directed to produce three-dimensional confined structures to fundamentally overcome the dipole selection rule for optical transition and to increase the carrier lifetime of the detector. Among different approaches, the quantum grid infrared photodetector (QGIP) structure has been proposed,<sup>6</sup> in which additional lateral confinement in a QWIP structure is achieved by patterning the active material into either a lamellar grid or a crossed grid structure. In addition to the expected intrinsic normal incident absorption from the lateral quantization, the grid also serves as a diffraction grating to direct part of the incident light into parallel propagation. With light coming into the detector material from all directions, intersubband transitions in all directions can occur simultaneously, leading to a potentially larger quantum efficiency and a wider absorption width. Fig. 21 is the SEM micrographs of typical QGIP devices.

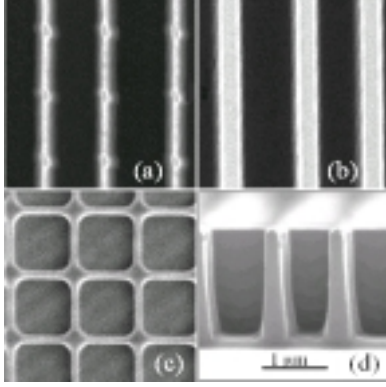


Fig. 21 SEM micrographs of QGIP devices with (a) dotted, (b) lamellar and (c) crossed grid patterns. In (d) cross section of the linear grid QGIP is shown. All images are  $3\mu\text{m} \times 3\mu\text{m}$ .

Fig. 22 shows the ratio of NR between a lamellar QGIP and the  $45^\circ$  edge-coupling sample from two wafer materials. This ratio is a measure of the improvement upon the standard coupling. In this experiment, we fix the spacing between the grid lines to be  $1.0\mu\text{m}$  and vary the line width  $w_1$  from  $0.1$  to  $4.0\mu\text{m}$ . Since there is electron depletion at the sidewalls of the exposed lines, we expect the actual line width of the thinnest line to be much smaller than  $0.1\mu\text{m}$ , and the effects of lateral electron confinement to be significant. For the QGIPs (represented by  $\Delta$ ) from one of the wafers, the NR ratio is peaked at  $w_1 = 1.5\mu\text{m}$  and  $4.0\mu\text{m}$ , respectively. These two values of  $w_1$  are predicted by the grating equation for the first- and second-order diffraction at  $90^\circ$  with  $\lambda = 7.6\mu\text{m}$ , which is the absorption peak of the detector material. The grid in this case acts as an efficient diffraction grating. On the other hand, the rise of the NR ratio below  $w_1 = 0.5\mu\text{m}$  for both wafers is unexplained by EM field modeling. We attribute this increase to the onset of the lateral electron confinement effects that allow intrinsic normal incident absorption and the increase of the photoconductive gain.

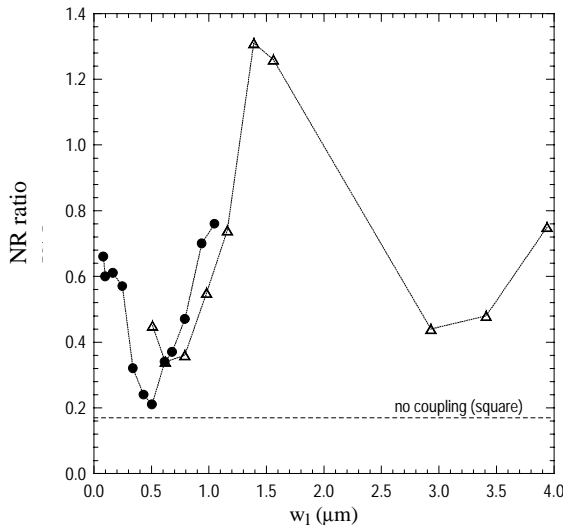


Fig. 22 The NR ratio of a QGIP as a function of line width of the grid. NR ratio = 1 means the corresponding QGIP has the same value of NR as the edge coupling QWIP.

We have tried to further improve the grid coupling efficiency using different grid sidewall profiles, similar to the C-QWIP concept.<sup>7</sup> In grating design, it is well known that a blaze reflection grating can shift the optical power from the usual zeroth-order diffraction to the first-order by choosing  $2\gamma = \theta$ , where  $\gamma$  is the blaze angle and  $\theta$  is the first-order diffraction angle. The flexibility of QGIP processing allows arbitrary values of period  $P$  and  $\gamma$  to be fabricated by directing the reactive ion beam at an oblique angle during material etching. With a proper blazed QGIP (BQGIP) design, a higher coupling efficiency is expected. Fig. 23 shows the BQGIPs with both lamellar and crossed grid patterns. In this experiment,  $\gamma$

is chosen to be  $60^\circ$  and the line spacing is fixed at  $1.5 \mu\text{m}$ , while the line width  $w_1$  is varied. With the lamellar BQGIP design (represented by diamonds), the NR ratio can be improved to 2.2 at  $P = 3.3 \mu\text{m}$ , which is larger than the value of 1.2 achieved by the standard QGIP (represented by circles), showing the advantage of a blaze design. We have also measured two BQGIPs with crossed grid design, the values of the NR ratio are 2.2 and 2.7 for  $w_1 = 0.7 \mu\text{m}$  and  $1.0 \mu\text{m}$ , respectively. Further improvements are expected when the period of the cross grid detector is optimized.

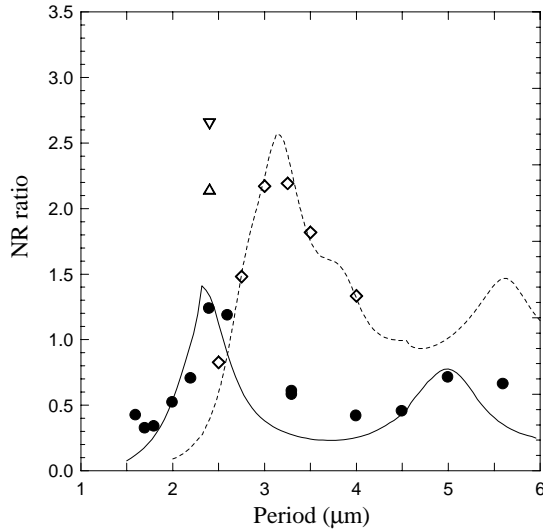


Fig. 23 The measured NR ratio of the standard lamellar QGIPs (●) and the lamellar blazed QGIPs (◊) as a function of  $P$ . The solid and dashed curves are from EM modeling without adjustable parameters. (Δ) and (▽) are experimental points for BQGIPs with crossed grid patterns for  $w = 0.7 \mu\text{m}$  and  $1.0 \mu\text{m}$  respectively.

## 8. ELECTROMAGNETIC FIELD MODELING FOR QWIPs

To understand and optimize the performance of a QWIP under a light coupling scheme, EM field modeling is an indispensable part of the research. In most cases, a detailed distribution of the electric field component  $E_x$  within the active volume is required to evaluate the efficiency of a particular coupling scheme. The knowledge of this spatial distribution becomes more critical when there are many reflecting surfaces within a grating unit cell that tend to localize the optical intensity in specific regions. The performance of a detector in this case depends on the relative locations of these intensity maxima and the active material, and does not follow an obvious relationship with the structural parameters of the coupling element. The obvious and important exception to this rule is of course that of the C-QWIP structures. The nearly  $45^\circ$  sidewalls in C-QWIPs produces vertical interference fringes that just become more or less densely populated for different incident wavelengths. The optical intensity upon spatial averaging remains constant, which forms the basis for wavelength independent detection.

On the other hand, other coupling schemes such as that of QGIPs are highly dependent on the coupling structural parameters and the wavelengths. In order to carry out the detector optimization effectively, an efficient and physically intuitive EM field modeling technique has to be sought. Among different EM field simulation techniques, the modal expansion techniques have been very successful in providing both rigorous numerical solutions and important physical insight into problems involving periodic structures. Recently, Tamir and Zhang developed a modal transmission-line theory<sup>8</sup> for multilayer grating structures, which is particularly suitable for the present research. This theory can yield rigorous numerical solutions with a personal computer and yet provides important physical insight into the effects of each reflecting surface. In this theory, a general solution of the EM field in every material layer including the grating region is expressed in the form of rigorous modal expansions. Each field mode consists of a summation over all the diffracted orders generated by the grating. Appropriate boundary conditions are set up at all interfaces to match each diffraction order across every interface. The problem can then be cast into and solved by an equivalent transmission-line network that provides transfer

matrices expressing input-output field relationship in every material layer. In this framework, the EM field distribution generated by the incident infrared radiation is obtained successively from layer to layer by matrix multiplication.

Although the original theory was developed for lamellar dielectric gratings with rectangular profiles, it can be readily extended to those with arbitrary (lamellar) sidewall profiles and to situations involving metal grating strips.<sup>9</sup> For the present detectors with different sidewall profiles, we partitioned the coupling structure horizontally into a sufficiently large number (twenty or more) of sublayers so that each sublayer can be approximated by a rectangular grating. In Fig. 3, we have already shown the  $I_x$  distribution associated with perpendicular electric field  $E_x$  in a C-QWIP structure. In Fig. 24, we show the  $|E_x|$  distribution for an optimized BQGIP at  $P = 3.3 \mu\text{m}$ . The coupling efficiency of the structure is evaluated by comparing the spatially averaged  $|E_x|^2$  within the active region to that of the edge coupling detector. The calculated coupling efficiency is plotted in Fig. 23.

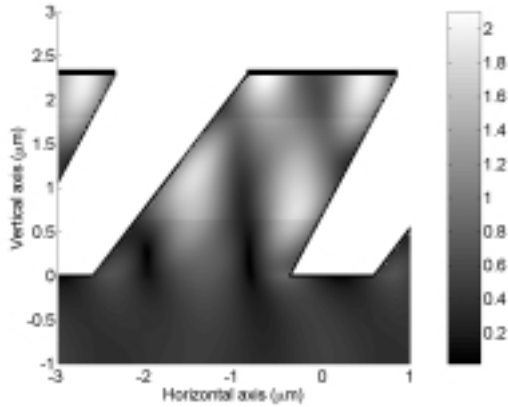


Fig. 24  $|E_x|$  distribution for  $\lambda = 7.6 \mu\text{m}$  in a BQGIP with  $P = 3.2 \mu\text{m}$ . Metal is assumed on top of the grid (thick line). The discontinuity of the field lines at  $y = 0.65 \mu\text{m}$  and  $1.8 \mu\text{m}$  is due to the small change in the dielectric constant between the GaAs contact layers and the GaAs/AlGaAs multiple quantum wells. The etching depth is  $2.3 \mu\text{m}$ .

From Fig. 24, it is apparent that the above structure provides optimum coupling because the structure creates intensity maxima within the active region. In Fig. 25, we show two otherwise identical structures except that one is covered with metal at the top of the lines (with sidewalls uncovered). The metal coverage intensifies  $|E_x|$  near the metal layer so that the peak intensity increases from 2.4 to 3.5. However, the enhancement is inside the detector contact region where no photocurrent is produced. The average intensity within the active region turns out to be actually reduced from 1.92 to 1.03 if metal is deposited relative to the incident polarized intensity. As a result, this apparently minor difference can affect the detector performance by a factor of two. Of course, once the field distribution is known, the performance of the detector with metal is easily be improved by having a much thinner top contact layer. This example shows the importance of EM modeling in understanding the detector performance.

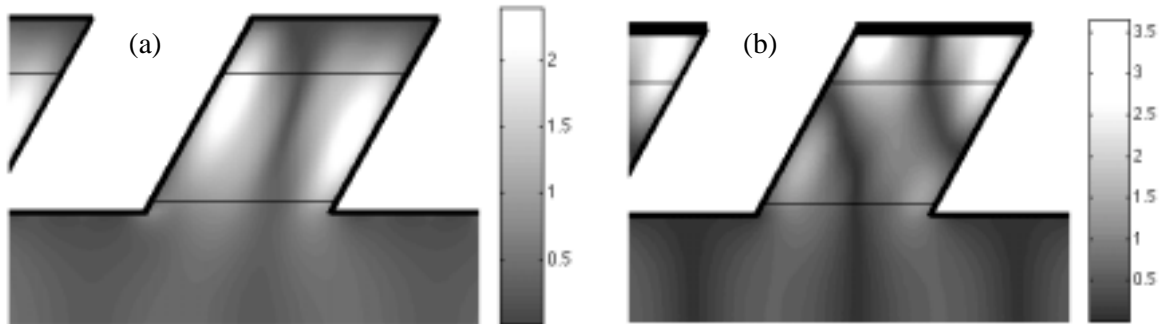


Fig. 25 Contours of  $|E_x|$  for  $P = 3.2 \mu\text{m}$  in the BQGIP (a) without metal and (b) with metal. The quantum well region is between the two thin horizontal lines. The etching depth is  $1.75 \mu\text{m}$ .

## 9. C-QWIP FOCAL PLANE ARRAYS

The performance of C-QWIPs has been substantiated in the detector array format.<sup>2,10</sup> In particular, FPAs with cutoff wavelength of 11.2 and 16.2  $\mu\text{m}$  have been fabricated and tested. In addition to the reduction of dark current, the measured internal quantum efficiency remains to be high, being 20.5 % and 25.4 % at 2 V bias for the 11.2  $\mu\text{m}$  and the 16.2  $\mu\text{m}$  FPA, respectively, confirming the theoretical and experimental results from the previous sections. The corresponding dark current limited  $D^*$  is  $2.6 \times 10^{11} \text{ cm}^2/\text{Hz}/\text{W}$  at 63 K for the 11.2  $\mu\text{m}$  FPA and  $2.0 \times 10^{11} \text{ cm}^2/\text{Hz}/\text{W}$  at 42 K for the 16.2  $\mu\text{m}$  FPA. Fig. 26 and shows the infrared imageries taking by the two FPAs.

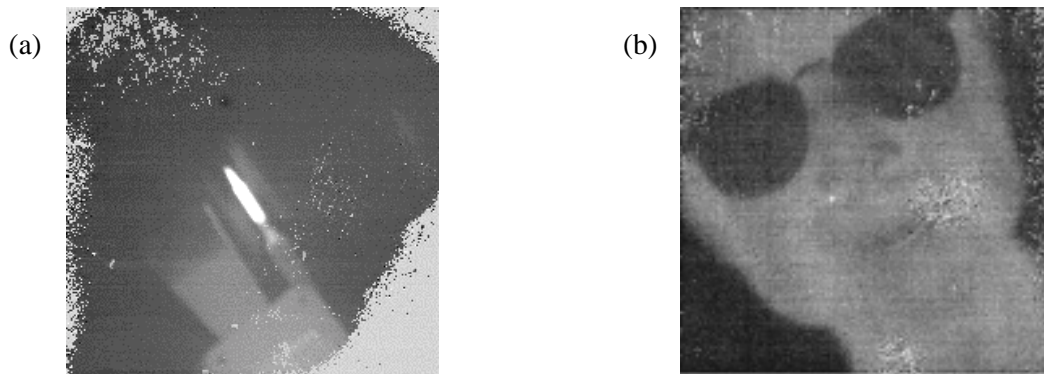


Fig. 26 IR imageries of (a) a 11.2  $\mu\text{m}$  C-QWIP FPA at 64 K and (b) a 16.2  $\mu\text{m}$  C-QWIP FPA at 38 K.

In conclusion, we have presented the current status of the C-QWIP technology. Further research and development are underway. Improved detector design and new array functionality are expected in the near future.

### REFERENCES:

1. C. J. Chen, K. K. Choi, W. H. Chang, and D. C. Tsui, Appl. Phys. Lett., 71, 3045 (1997).
2. K. K. Choi, C. J. Chen, A. C. Goldberg, W. H. Chang and D. C. Tsui, (SPIE 3379, 441, 1998) SPIE AeroSense, Orlando FL, 13-17 April 1998.
3. C. J. Chen, K. K. Choi, W. H. Chang, and D. C. Tsui, Appl. Phys. Lett., 72 7 (1998).
4. C. J. Chen, K. K. Choi, L. Rohkinson, W. H. Chang, and D. C. Tsui, Appl. Phys. Lett., 74 862 (1999).
5. K. K. Choi, K. L. Bacher and Y. Wu, Proceedings of the 6<sup>th</sup> International Symposium on Long Wavelength Infrared Detectors and Arrays: Physics and Applications (Li, Liu Tidrow and Gunapala eds. New Jersey: The Elect. Chem. Society, Inc) p. 71 (1998).
6. L. P. Rokhinson, C. J. Chen, D. C. Tsui, A. G. Vawter, and K. K. Choi, Appl. Phys. Lett., 74 759 (1999).
7. L. P. Rokhinson, C. J. Chen, K. K. Choi, D. C. Tsui, A. G. Vawter, L. Yan, M. Jiang, and T. Tamir, submitted to Appl. Phys. Lett.
8. T. Tamir and S. Zhang, J. Lightw. Technol. 14, 914 (1996).
9. L. Yan, M. Jiang, T. Tamir and K. K. Choi, submitted to IEEE Journal of Quantum Electronics.
10. N. C. Das, K. K. Choi, A. C. Goldberg, A. La, M. Jhabvala, R. B. Bailey and K. Vural, SPIE (3698, 1999) SPIE AeroSense, Orlando, FL April 5-9, 1999.